

Article

Slot-Die-Coated Active Layer for Printed Flexible Back-Contact Perovskite Solar Cells

Hryhorii P. Parkhomenko , Mayuribala Mangrulkar  and Askhat N. Jumabekov * 

Department of Physics, School of Sciences and Humanities, Nazarbayev University, Astana 010000, Kazakhstan

* Correspondence: askhat.jumabekov@nu.edu.kz

Abstract: Perovskites have already shown potential as active layers in photovoltaic applications. Furthermore, a low-cost and simple solution processing technology allows perovskites to be used in flexible and printed electronics. Perovskite solar cells (PSC) with a back-contact (BC) structure, in which the electrode system is based on a quasi-interdigitated back-contact (QIBC) design, promise to increase the power conversion efficiency (*PCE*) of devices beyond those that can be obtained using PSCs with a traditional sandwich structure. While the spin-coating technique is used to deposit the perovskite layer of lab-scale BC PSCs, the application of large-area printing techniques to deposit the perovskite layer of such devices is yet to be explored. Therefore, this work demonstrates an application of the slot-die coating technique to print the perovskite active layer of BC PSCs with QIBC electrodes on flexible polymer substrates. The morphology of the obtained perovskite films on QIBC electrodes are investigated and the primary photoelectric parameters of the resulting BC PSCs are measured. The charge carrier recombination processes in the fabricated BC PSCs are investigated and the dominant mechanism for carrier loss in the devices is determined. The findings of the work give an insight into the properties of the slot-die-coated perovskite active layer of BC PSCs and points to exciting new research opportunities in this direction.

Keywords: perovskite solar cell; back-contact; slot-die coating; flexible substrates; QIBC



Citation: Parkhomenko, H.P.; Mangrulkar, M.; Jumabekov, A.N. Slot-Die-Coated Active Layer for Printed Flexible Back-Contact Perovskite Solar Cells. *Coatings* **2023**, *13*, 550. <https://doi.org/10.3390/coatings13030550>

Academic Editors: Fausta Loffredo and Fulvia Villani

Received: 20 January 2023

Revised: 24 February 2023

Accepted: 1 March 2023

Published: 3 March 2023



Copyright: © 2023 by the authors. Licensee MDPI, Basel, Switzerland. This article is an open access article distributed under the terms and conditions of the Creative Commons Attribution (CC BY) license (<https://creativecommons.org/licenses/by/4.0/>).

1. Introduction

In recent years, perovskites—compounds that have an ABX_3 crystal structure, in which “A” is an organic and/or inorganic cation, “B” is a bivalent metal cation, and “X” is an anion—have attracted a significant interest in the field of optoelectronics due to their excellent material properties [1–3]. One of the most studied perovskites for optoelectronic applications is methylammonium lead iodide ($MAPbI_3$). This is due to high light absorption [4,5], low exciton binding energy [6], and optimal band gap (1.55 eV) [7–9] of $MAPbI_3$, which makes it well-suited for use in solar energy conversion devices. In addition, the manufacturing of perovskite solar cells (PSCs) is relatively simple and cost-effective, and the obtained devices are highly efficient [10,11]. Currently, the highest obtained power conversion efficiency (*PCE*) for PSCs is about 25.7% [12].

Typically, PSCs are fabricated on rigid glass substrates [13,14]. This is due to the high-temperature processing requirements of inorganic semiconductor materials to prepare the device functional layers (e.g., the electron and hole-transporting layers (ETLs and HTLs) and the metallic contacts). Recent advances in obtaining inorganic device functional layers at low processing temperatures (<150 °C) [15] have enabled the fabrication of PSCs on flexible polymer substrates. (e.g., polyethylene terephthalate (PET), polyethylene naphthalate (PEN), etc.) [16]. The use of flexible substrates in combination with the possibility of solution processing of some or all device functional layers has led to significant advancements in manufacturing of PSCs [17–19]. This allows for a cost-effective and simple manufacturing process to scale-up the production of PSCs [20,21].

Slot-die coating is a promising technique for solar cell production as it provides a simple and fast deposition of uniform and continuous thin films of solution-processed

materials with various structures and viscosities [15,16]. Thin films can be deposited both on rigid and flexible substrates, employing sheet-to-sheet as well as roll-to-roll coating modes [21]. This allows the high-speed production of printed devices at lower manufacturing costs, which makes it an attractive technique for the commercial production of PSCs and other optoelectronic devices [22]. In recent years, the fabrication of slot-die-coated PSCs has improved significantly, reaching *PCEs* of over 20% in devices [23].

The architecture of solar cells is also evolving. The so-called “sandwich” structure is the most employed structure of devices in PSCs. The device functional layers (perovskite active layer, ETL, HTL, and metallic contacts) are deposited sequentially in this type of devices, resembling a sandwich-like structure [24]. Another more promising device structure for PSCs is the back-contact (BC) structure and the corresponding devices are referred to as BC PSCs [25]. Here, the entire electrode system of devices is placed on only one side of the perovskite active layer. This reduces transmission losses in devices and promises to result in higher *PCEs* [25].

In 2016, a new design for BC electrodes, which are referred to as quasi-interdigitated back-contact (QIBC) electrodes, was proposed by Jumabekov et al. to fabricate BC PSCs [26]. The QIBC design of the electrode system of BC PSCs is found to be an effective and relatively easy-to-manufacture when compared to other BC electrode designs proposed by other groups [27]. Here, a microfabricated anode layer is placed on top of a continuous cathode layer (or vice versa), while the perovskite active layer is deposited over the whole electrode system. The advantage of the QIBC design is that it affords a wider optical response range in BC PSCs and the issue of light transmission losses in the device functional layers, which is inherent in PSCs with sandwich structures, is eliminated, since the incident light enters the perovskite layer of BC PSCs directly [28]. Additionally, the back-contact structure in PSCs allows for the prefabrication of the electrode system prior to deposition of the perovskite active layer, which is convenient for their long-term storage and transportation. Once fabricated, the perovskite active layer can be deposited on the BC electrode system at any time, using various deposition methods such as spin-coating, printing, thermal evaporation, etc. Currently, only a few studies have demonstrated the ability to manufacture flexible solar cells with back-contact structures and the highest reported *PCE* (~11%) was obtained in BC PSCs employing the QIBC design for the BC electrode system [29]. The reported works in the literature use the spin-coating technique to deposit the perovskite layer of flexible BC PSCs. However, this technique restricts the upscaling of the device manufacturing process [30]. The slot-die coating technique, on the other hand, is a widely used technique for printing of large-area flexible PSCs and is suitable for scale-up manufacturing. Thus, combining printing techniques for flexible substrates with BC electrodes for PSCs may improve the device functionality while simplifying the manufacturing process.

In this work, BC PSCs were fabricated by depositing the perovskite active layer on the prefabricated QIBC electrodes on flexible substrates using the slot-die coating technique. The surface morphology of the prepared electrode system and the printed perovskite active layer were investigated. The main photoelectric parameters of the obtained flexible quasi-interdigitated back-contact perovskite solar cells (PFQIBC PSCs) were investigated and the dominant recombination mechanism for carrier loss in the devices was determined.

2. Materials and Methods

2.1. Materials

PET substrates with a patterned indium-tin oxide (ITO) layer (thickness of PET~125 μm , ITO~150 nm; sheet resistance: 48 Ω/sq) were purchased from Mekoprint (Stovring, Denmark). Acetone and lead (II) iodide (PbI_2 , 99.0%) were purchased from Sigma-Aldrich (St. Louis, MO, USA). Methylammonium iodide (MAI) ($\text{CH}_3\text{NH}_3\text{I}$, 99.99%) was purchased from Greatcell Energy (Perth, W.A., Australia). Methylamine solution (MA, in absolute ethanol 33 wt.%) and acetonitrile (ACN, 99.8%) were purchased from Merck (St. Louis, MO, USA). AZ 726 MIF developer and AZ 1518 photoresist were purchased from Microchemicals GmbH (Ulm, Germany).

2.2. Device Fabrication

The PET/ITO substrates were cleaned for 15 min in an ultrasonic bath with detergent, deionized water, acetone, and ethanol. A 30 nm SnO₂ layer was deposited as the ETL on the substrates using the radio frequency magnetron sputtering technique (Spectros, Kurt J. Lesker, Jefferson Hills, PA, USA). Then, a sacrificial polymer mask for the second electrode was created through a photolithography process, in which a positive photoresist layer was spin-coated at 4000 RPM for 30 s, baked for 2 min at 110 °C, and exposed to UV light (400 nm, 210 mJ/cm²) using a SUSS MicroTec (Garching, Germany) MA/BA Gen4 mask aligner and a photomask. The exposed areas of the photoresist layer were then removed by rinsing the substrates in a developer solution (AZ 726 MIF mixed with water, 3:1) for 30 s. Finally, the substrates were rinsed in water.

The second electrode was fabricated on the substrates through a sequential deposition of an Al₂O₃ insulating layer (100 nm), a chromium layer (10 nm), and a gold layer (70 nm) using an electron beam evaporator (Nexdep PVD, Angstrom Engineering Inc., Kitchener, Canada). The thickness of the layers was controlled using a crystal quartz monitor during the deposition process, and was confirmed using a profilometer (Dektak XT Stylus Profiler, Bruker, Billerica, MA, USA). The gold layer of the second electrode serves as the metallic contact of the anode layer. After, the remainder of photoresist was removed from the substrates by rinsing them with acetone (the lift-off process), resulting in QIBC electrodes ready to use for the fabrication of PFQIBC PSCs. It should be noted that the QIBC electrode system for PFQIBC PSCs does not have the HTL, i.e., hole extraction in devices relies on a Schottky junction between the perovskite layer and the gold layer of the QIBC electrode system. The detailed process of electrode fabrication is depicted in Figure S1 in the Supplementary Materials. A photo-image of the prefabricated QIBC electrodes on the PET/ITO substrate is shown in Figure 1.

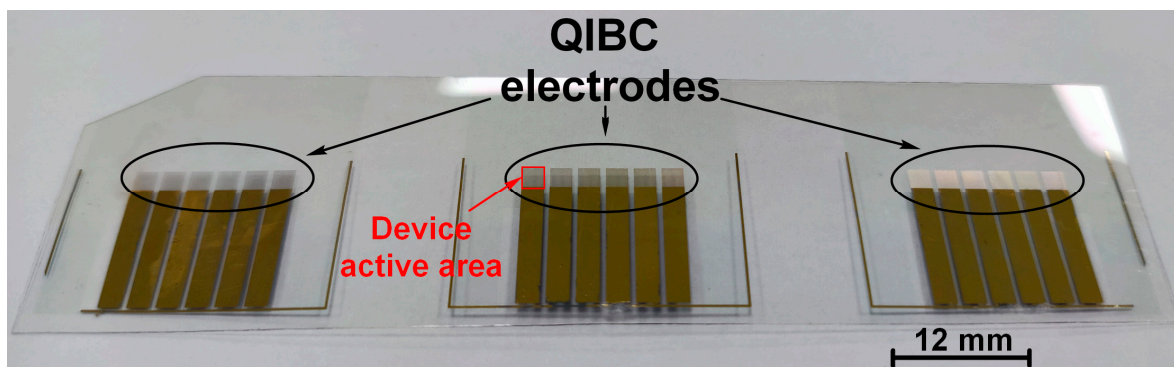


Figure 1. A photo-image of prefabricated QIBC electrodes on PET/ITO substrate.

The final step in the PFQIBC PSC fabrication process is the deposition of the perovskite photoactive layer using the slot-die coating technique. The MAPbI₃ precursor inks were prepared by dissolving 1 mol of MAI (159 mg) and PbI₂ (461 mg) in 0.7 mL of MA and 0.7 mL of ACN [31]. The MAPbI₃ layer was slot-die coated on the freshly prepared QIBC electrodes using a slot-die coater (Vector, FOM Technologies, Copenhagen S., Denmark). The ink pump rate and the coating speed of the perovskite layer were 0.15 mL/min. After the deposition of the perovskite layer, the substrates were annealed at 100 °C for 10 min. The schematic representation of the slot-die coating process of the perovskite active layer, photo image of the slot-die coating process, and fabricated devices are shown in Figure 2a–c, respectively. The deposition of the perovskite layer and all measurements were carried out in ambient conditions without changing the parameters during the measurements.

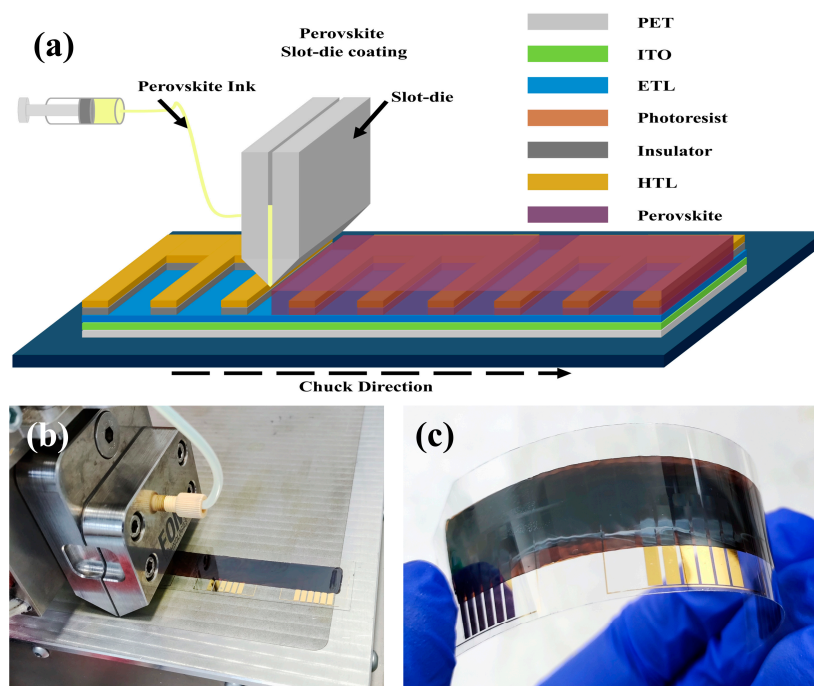


Figure 2. (a) Schematic representation of the perovskite layer fabrication process for PFQIBC PSCs; (b) and (c) are the photo-images of the slot-die coating process and fabricated devices, respectively.

2.3. Device Characterization

The surface images of the electrodes and perovskite layer were obtained with a scanning electron microscope (Crossbeam 540, Zeiss, Jena, Germany). AFM measurements were conducted using an Atomic Force Microscope SmartSPM 1000 (SmartSPM 1000, AIST-NT, Novato, CA, USA). The crystal structure of the perovskite layers was examined using an X-ray diffractometer (XRD, SmartLab Rigaku, Austin, TX, USA) with a $\text{Cu K}\alpha = 1.5418 \text{ \AA}$ X-ray beam. The photoluminescence (PL) spectra of the printed perovskite films were analyzed using a spectrometer (FLS 1000, Edinburgh Instruments, Livingston, UK) with a 405 nm laser. The absorbance spectra of the printed perovskite films were measured using a UV-vis-NIR spectrophotometer (Lambda 1050, Perkin Elmer, Waltham, MA, USA). The active area of the devices was 0.04 cm^2 and corresponded to the area of the QIBC electrodes (see red rectangle in Figure 1). This was measured and confirmed (see Figure S2 in Supplementary Materials) for all tested devices using a photocurrent mapping system (LBIC, InfinityPV ApS, Jyllinge, Denmark). The J - V curves were measured in ambient conditions under AM1.5G solar irradiation at 100 mW/cm^2 using a solar simulator (ORIEL Sol3A, Newport, Irvine, CA, USA) and a parameter analyzer (B1500A, Keysight, Santa Rosa, CA, USA). The open-circuit voltage decay (OCVD) was measured using a potentiostat/galvanostat system (Autolab PGSTAT302N, Metrohm, Herisau, Switzerland).

3. Results and Discussions

The quality of the slot-die-coated perovskite films on PET was checked using XRD, PL, and UV-Vis transmittance measurements. The XRD pattern of a freshly prepared MAPbI_3 perovskite film shows that the film is crystalline and the perovskite material has a tetragonal phase [10]. The XRD pattern of the measured perovskite film indicated the presence of a small amount of PbI_2 in the bulk of the film (see Figure S3 in Supplementary Materials). This could be due to unreacted PbI_2 precursor or some degradation of the film during the measurements [10]. Figure 3 shows the measured spectra for PL emission and UV-vis-NIR absorbance in a slot-die-coated MAPbI_3 film. The position of the PL peak maximum indicates that the band gap of the MAPbI_3 is 1.59 eV, which is consistent with the band gap of the tetragonal phase MAPbI_3 at room temperature [4].

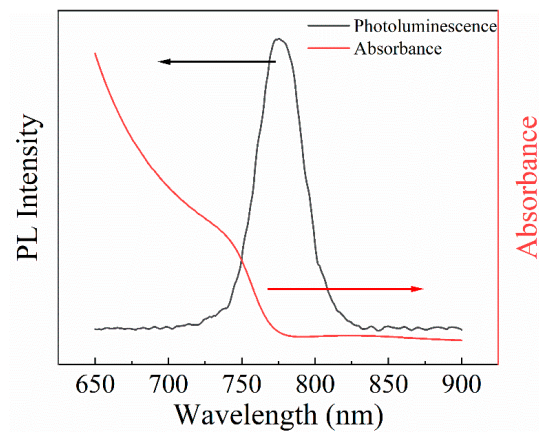


Figure 3. Absorbance and photoluminescence spectra of a printed perovskite film on PET substrate.

While the quality of the perovskite active layer has a significant impact on the photovoltaic parameters of solar cells, the anode and cathode layers are critical in the transport of charge carriers. Therefore, the changes in the morphology of these layers during fabrication of QIBC electrodes were investigated. Figure 4 depicts the SEM and AFM images of the surface morphology of the SnO_2 ((a) and (d)), Au ((b) and (e)), and the top view of the QIBC electrode system prior to the deposition of the perovskite layer ((c) and (f)), respectively.

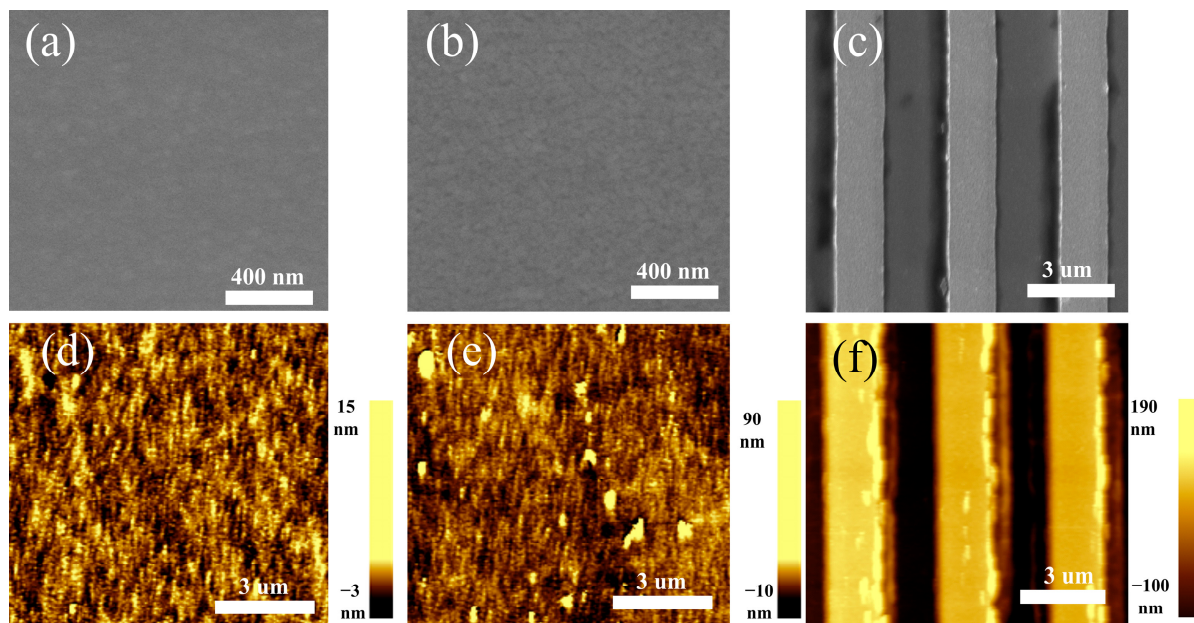


Figure 4. SEM top view and AFM images of the SnO_2 layer (a,d), Au layer (b,e), and the QIBC electrode system (c,f).

The SnO_2 and Au layers have root mean square (RMS) values of 12.9 and 23.4 nm, respectively, and were estimated using an atomic force microscope (AFM). This indicates that the anode and cathode layers are smooth without any significant defects (Figure 4d,e). The SEM images also confirm the good quality of the anode and cathode layer, which are free of pinholes and defects (Figure 4a,b). The fabricated QIBC electrodes were also of good quality as there were almost no defects after the lift-off process and the top electrode features were not broken (Figure 4c,f).

The surface morphology of a slot-die-coated perovskite layer on top of a flexible QIBC electrode system on PET/ITO was examined using the AFM and SEM techniques. Figure 5 shows that the perovskite layer completely covers the surface of the electrodes (Figure 5a,d).

The roughness value of the perovskite film appears slightly more than that of the HTL (RMS = 23.9 nm). Furthermore, the presence of small crystallites is noticeable, which could be attributed to the perovskite film deposition process. Regardless of this, the perovskite layer appears to coat the surface of the QIBC electrodes evenly (Figure 5c). The observed wavy concavity pattern on the AFM image shown in Figure 5f is due to the texture of the QIBC electrodes.

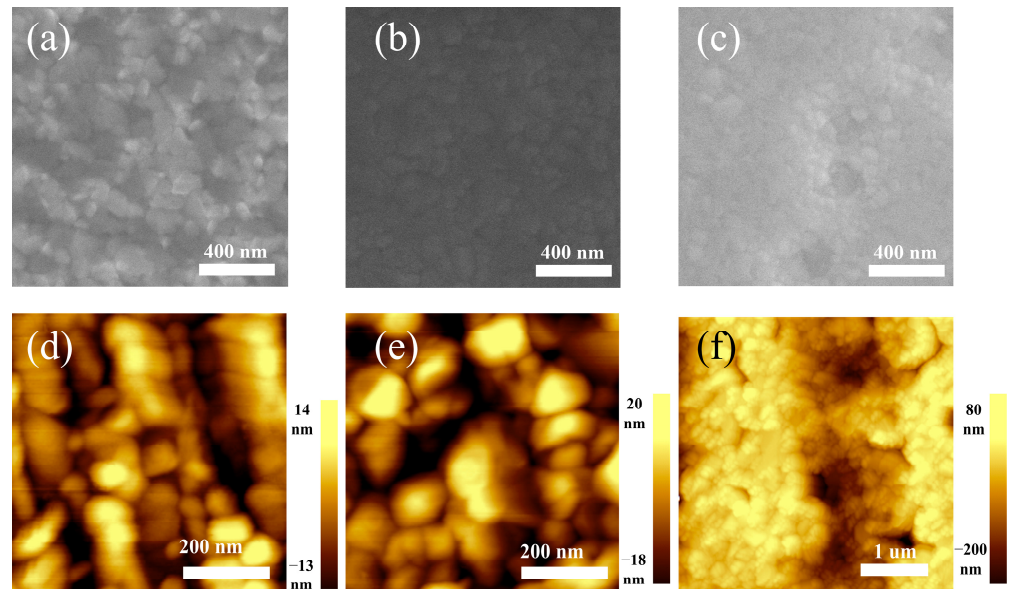


Figure 5. SEM top view and AFM images of a perovskite film on the ETL layer (a,d), HTL layer (b,e), and the QIBC electrodes (c,f), respectively.

Figure 6 depicts the measured current density-voltage (J - V) characteristic curves of an experimentally obtained PFQIBC PSC. The J - V curves indicate that the tested device has a low hysteresis index value of 0.22. (See Figure 6). The open-circuit voltage (V_{oc}), short-circuit current (J_{sc}), fill factor (FF) and PCE of the device extracted from the J - V curves are shown in Table 1. The prepared devices did not show a visible sign of degradation after storing them in a dry nitrogen atmosphere for the duration of 1 month. However, a comprehensive study to assess the stability of the prepared devices [32,33] was not conducted within the scope of this work.

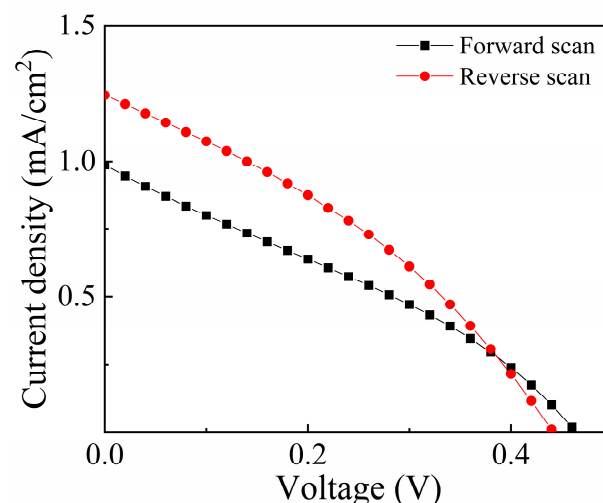


Figure 6. J - V curves of a PFQIBC PSC under AM1.5G solar irradiation.

Table 1. The photovoltaic parameters of a PFQIBC PSC under AM1.5G solar irradiation.

| Scan Direction | V_{oc} , V | J_{sc} , mA/cm ² | FF, % | PCE, % |
|----------------|--------------|-------------------------------|-------|--------|
| Reverse | 0.44 | 1.24 | 34 | 0.18 |
| Forward | 0.46 | 0.98 | 33 | 0.14 |

In order to gain some understanding of the performance limitations in the fabricated PFQIBC PSCs, devices with a sandwich structure (see Figure S4 in Supplementary Materials) were also fabricated using the same deposition parameters for the functional layers of devices. Figure S4 and Table S1 in the Supplementary Materials present the J - V curves and main photovoltaic parameters of the device. Compared to the PFQIBC PSC, the device with the sandwich structure exhibited a slightly lower V_{oc} , but comparable FF values. The J_{sc} of the sandwich device, on the other hand, was significantly higher than the J_{sc} of the PFQIBC PSC device. Due to this, the PCE values of the sandwich device were also higher than that of the back-contact structure. This major difference in the J_{sc} of sandwich- and back-contact-structured devices is because in the former, the photo-generated charge carriers, in general, move in a ‘vertical’ direction along the thickness of the perovskite layer to reach their respective charge collecting layers (SnO₂ and Au in this work). A typical thickness of the perovskite layer in most sandwich-structured devices is around 0.5 μm. This is the maximum distance that the photo-generated charge carriers must travel to reach their respective carrier collecting layers. We note that a value of 0.5 μm is comparable to the value of diffusion length of charge carriers in most perovskite films obtained using typical deposition techniques in PSC fabrication. As for PSCs with a back-contact structure, charge carriers need to move in both ‘vertical’ and ‘lateral’ directions within the perovskite layer to reach their respective carrier-collecting layers. In our case, the maximum distance that charge carriers have to travel within the perovskite layer to reach their respective charge collecting layers is around 2 μm. This length is significantly larger than the carrier diffusion length in typical perovskite films. Hence, the recombination rate of charge carriers in the back-contact-structured devices reported within this work is expected to be high when compared to devices with sandwich structures. This is evident in our findings, in which the J_{sc} of the sandwich structured device was a factor of 4.8 higher than the J_{sc} of the back-contact-structured device (see Table 1 and Table S1 in Supplementary Materials). To mitigate the low J_{sc} issue in back-contact PSCs, carrier diffusion length in the perovskite layer must be comparable or larger than the maximum distance that the photo-generated charge carriers must travel to reach their respective charge collecting layers [26]. This can be achieved by increasing the average size of the perovskite layer crystallites and ensuring the low concentration of defects within the bulk and surface of the perovskite active layer [34].

Open-circuit voltage decay measurements were performed to analyze the changes in V_{oc} and the dominant recombination losses in the devices. Figure 7a shows the V_{oc} decay curve for a PFQIBC PSC. The V_{oc} of the device decays almost completely within 10⁻² s. The relationship between the carrier recombination lifetime (τ) and the V_{oc} decay under a high carrier excitation condition is described by the following expression [35,36]:

$$\tau = -\frac{kT}{q} \left(\frac{dV_{oc}}{dt} \right)^{-1} \quad (1)$$

Here, k is Boltzmann’s constant, T is the absolute temperature, and q is the unit charge.

The inset in Figure 7a depicts the calculated τ as a function of time. It indicates that τ gradually increase with time, indicating that one recombination mechanism is dominant in the studied interval after the illumination is turned off [37]. Figure 7b shows an analysis of the recombination lifetime of the device in relation to the open-circuit voltage. The results indicate that the recombination lifetime at higher voltages ($V_{oc} > 0.15$ V) decays more quickly than it does at lower voltages ($V_{oc} < 0.15$ V). This may be due to the presence of traps in the perovskite layer and the discharge of charge carriers at lower voltages. The next step involves identifying the dominant recombination mechanisms and gaining insights

into their relative contributions to the total recombination loss. The effective recombination index (β) can be determined from expression (2) and is presented as [37,38]:

$$\beta = 1 + \frac{kT}{q} \frac{d \ln \tau^{-1}}{dV_{oc}} \quad (2)$$

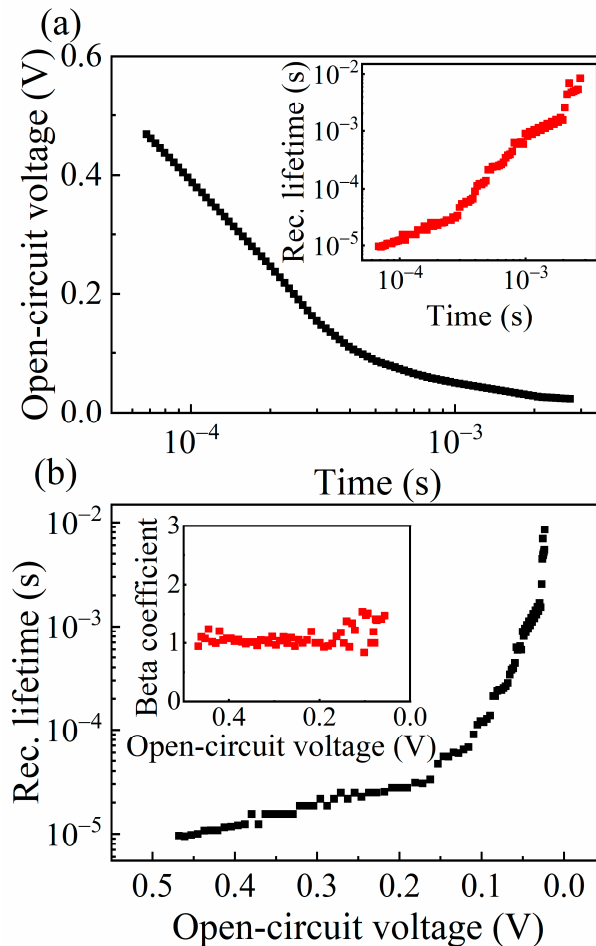


Figure 7. (a) Open-circuit voltage decay; the inset shows the recombination lifetime (τ) as a function of time. (b) τ vs. V_{oc} ; the inset shows the dependence of β on V_{oc} .

The inset graph in Figure 7b shows the dependence of β on V_{oc} . An almost unchanged value (~ 1) for β indicates that the Shockley–Read–Hall (SRH) recombination is the dominant mechanism contributing to the carrier loss in the tested PFQIBC PSC [37].

Since the perovskite layer deposition was completed in an ambient condition employing rapidly evaporating solvents (MA and ACN), the process of crystallization and growth of the perovskite film is difficult to control. As a result, highly polycrystalline perovskite films are obtained. Such perovskite films have many defects, particularly internal defects [39]. In our case, the dominant type of recombination loss is SRH recombination, which is due to traps forming internal defects. Internal or point defects in a semiconductor are classified as atomic vacancies, interstitial atoms, and substitutional atoms [39,40]. The ideal structure of MAPbI₃ has 12-point defects: MA, Pb, and I vacancies; MA, Pb, and I interstitials; and six substitutions which are MAPb, PbMA, MAI, PbI, IMA, and IPb [39,41]. The defects listed above create energy levels in the band gap and act as recombination centers. In addition to point defects, grain boundaries, which are also the recombination centers, have a considerable effect on the performance of devices [42,43]. The factors outlined above play a crucial role in the generation and collection of charge carriers by electrodes. In our particular case, it is highly probable that there are many defects at the

grain boundaries. These defects could have resulted in imperfections on the surface of the perovskite active layer and a reduction in the efficiency of the device by impeding the movement of charge carriers, especially in the lateral direction. Therefore, it is necessary to minimize the concentration of defects for the optimal performance of devices. It is noteworthy that the *PCE* of PFQIBC PSCs is also hindered by the utilization of the Schottky junction at the perovskite/gold interface as the extraction of holes from the perovskite layer. While PSCs employing Schottky junctions have shown some promising results, they have not yet reached the same *PCE* levels as those employing perovskite/HTL junctions. The highest reported *PCEs* for PSCs with Schottky junctions typically range from 9% to 11% [44,45], whereas PSCs with perovskite/HTL junctions can achieve *PCEs* exceeding 25% [12]. One reason for this is that the metal layer can act as a recombination center for charge carriers, reducing the overall efficiency of devices [28]. Additionally, the Schottky junction can introduce an additional resistance, lowering the fill factor and overall *PCE* of devices. One way to improve the performance of PSCs with Schottky junctions is to use molecular interlayers that can improve the surface property of the perovskite layer at the metal/perovskite interface and can also alter the work function of the metal, which can help to increase the V_{oc} of devices [46]. Ultimately, PSCs with Schottky junctions have the potential to be a low-cost and scalable alternative to PSCs with perovskite/HTL junctions.

Overall, it can be suggested that to increase the *PCE* of PFQIBC PSCs, it is necessary to obtain high quality perovskite active layers in devices [25,27]. We note that this is not a trivial task to accomplish even with the spin-coating technique that is commonly used to fabricate lab-scale PSCs [10,28,34]. Hence, using printing techniques (e.g., slot-die coating) to deposit high-quality perovskite films with large crystallites, reduced grain boundaries, and fewer defects can be rather challenging. This can be further complicated by conducting the printing processes in ambient conditions with uncontrolled humidity and temperature as it was in this work. On top of that, the textured nature of QIBC electrodes is another major hurdle that can prevent the deposition of high-quality perovskite films using printing techniques. Considering this, it is anticipated that the performance of back-contact PSCs with a printed perovskite photo-active layer might be low at this initial stage. Thus, a further optimization of both the back-contact electrode fabrication and printing processes is required to increase the *PCE* of PFQIBC PSCs. Nevertheless, these are intriguing and exciting new research challenges that need to be addressed to bring the PSC technology to its industrial and commercial level production. There are several ways to achieve this. First, this can be completed by employing more complex and advanced perovskite materials beyond MAPbI_3 , which are more stable and have suitable electronic properties [47,48]. Second, regarding the printing techniques, improvements can be implemented by employing a variety of slot-die printing methods that utilize anti-solvent [49,50] and air-knife [51] quenching strategies to deposit high-quality perovskite films. An additional boosting of the quality of slot-die-coated perovskite films is possible using various passivating agents and additives [52], coatings [46], and interlayers, which can be extremely useful in increasing the stability of the films in addition to their role in reducing recombination losses in the perovskite layer and at the HTL/perovskite and ETL/perovskite interfaces. Finally, the use of anti-reflective coatings on top of the perovskite layer in BC PSCs can help to increase the light harvesting ability of devices and help to boost their J_{sc} [53]. A successful realization of these strategies promise to enhance the performance of back-contact PSCs to a desired level and pave the way for their effective and timely application in energy conversion technologies [54].

4. Conclusions

In conclusion, the fabrication of printed flexible quasi-interdigitated back-contact perovskite solar cells using the slot-die coating technique has been demonstrated. AFM and SEM techniques were used to investigate the surface morphology of functional layers and the quality of fabricated QIBC electrodes. The photovoltaic parameters of the fabricated PFQIBC PSCs were determined from the *J-V* curves. Based on open-circuit voltage decay

measurements, it was determined that the Shockley–Read–Hall recombination mechanism is the primary recombination pathway for carrier loss in devices. The experimental findings indicate that the quality of the perovskite active layer needs to be optimized to further improve the performance of FQIBC PSCs. These findings could be applied to the development of multifunctional optoelectronic devices, as well as flexible and portable electronics for energy applications and other emerging technologies such as IoT technology.

Supplementary Materials: The following supporting information can be downloaded at: <https://www.mdpi.com/article/10.3390/coatings13030550/s1>, Figure S1: block diagram illustrating the process of PFQIBC PSC fabrication and a schematic diagram of the final device.; Figure S2: photocurrent map of PFQIBC PSCs. The data was taken with a laser of 410 nm wavelength; Figure S3: XRD pattern of a slot-die coated perovskite film on PET substrate; Figure S4: current-voltage characteristic curves of a printed and flexible perovskite solar cell with a sandwich structure. The inset graph shows a scheme of the device structure; Table S1: the photovoltaic parameters of a sandwich PSC under AM1.5G solar irradiation.

Author Contributions: Conceptualization A.N.J.; methodology, H.P.P. and A.N.J.; formal analysis, H.P.P. and M.M.; investigation, H.P.P. and M.M.; writing—original draft preparation, H.P.P. and A.N.J.; writing—review and editing, A.N.J. and M.M.; supervision A.N.J. All authors have read and agreed to the published version of the manuscript.

Funding: This research was funded by Research Grants from Ministry of Education and Science of the Republic of Kazakhstan (Grant Numbers: AP14869871 and AP08052412) and Nazarbayev University Collaborative Research Grant (Grant Number: 021220CRP1922).

Institutional Review Board Statement: Not applicable.

Informed Consent Statement: Not applicable.

Data Availability Statement: The data that support the findings of this study are available from the corresponding author upon reasonable request.

Conflicts of Interest: The authors declare no conflict of interest.

References

1. Mercier, N. Hybrid Halide Perovskites: Discussions on Terminology and Materials. *Angew. Chem. Int. Ed.* **2019**, *58*, 17912–17917. [[CrossRef](#)] [[PubMed](#)]
2. Yu, Y.; Huang, P.; Wang, Y.; Zhang, Z.; Zhang, T.; Zhang, Y.; Fu, D. X-Site Doping in ABX₃ Triggers Phase Transition and Higher T_c of the Dielectric Switch in Perovskite. *Chin. Chem. Lett.* **2021**, *32*, 3558–3561. [[CrossRef](#)]
3. Ali, N.; Shehzad, N.; Uddin, S.; Ahmed, R.; Jabeen, M.; Kalam, A.; Al-Sehemi, A.G.; Alrobei, H.; Kanoun, M.B.; Khesro, A.; et al. A Review on Perovskite Materials with Solar Cell Prospective. *Int. J. Energy Res.* **2021**, *45*, 19729–19745. [[CrossRef](#)]
4. Zhu, X.; Su, H.; Marcus, R.A.; Michel-Beyerle, M.E. Computed and Experimental Absorption Spectra of the Perovskite CH₃NH₃PbI₃. *J. Phys. Chem. Lett.* **2014**, *5*, 3061–3065. [[CrossRef](#)]
5. Al-Asbahi, B.A.; Qaid, S.M.H.; Hezam, M.; Bedja, I.; Ghaithan, H.M.; Aldwayyan, A.S. Effect of Deposition Method on the Structural and Optical Properties of CH₃NH₃PbI₃ Perovskite Thin Films. *Opt. Mater.* **2020**, *103*, 109836. [[CrossRef](#)]
6. Yang, Y.; Yang, M.; Li, Z.; Crisp, R.; Zhu, K.; Beard, M.C. Comparison of Recombination Dynamics in CH₃NH₃PbBr₃ and CH₃NH₃PbI₃ Perovskite Films: Influence of Exciton Binding Energy. *J. Phys. Chem. Lett.* **2015**, *6*, 4688–4692. [[CrossRef](#)]
7. Jeyakumar, R.; Bag, A.; Nekovei, R.; Radhakrishnan, R. Interface Studies by Simulation on Methylammonium Lead Iodide Based Planar Perovskite Solar Cells for High Efficiency. *Sol. Energy* **2019**, *190*, 104–111. [[CrossRef](#)]
8. Eperon, G.E.; Stranks, S.D.; Menelaou, C.; Johnston, M.B.; Herz, L.M.; Snaith, H.J. Formamidinium Lead Trihalide: A Broadly Tunable Perovskite for Efficient Planar Heterojunction Solar Cells. *Energy Environ. Sci.* **2014**, *7*, 982–988. [[CrossRef](#)]
9. Yan, J.; Song, X.; Chen, Y.; Zhang, Y. Gradient Band Gap Perovskite Films with Multiple Photoluminescence Peaks. *Opt. Mater.* **2020**, *99*, 109513. [[CrossRef](#)]
10. Zhang, B.; Zhang, M.-J.; Pang, S.-P.; Huang, C.-S.; Zhou, Z.-M.; Wang, D.; Wang, N.; Cui, G.-L. Carrier Transport in CH₃NH₃PbI₃ Films with Different Thickness for Perovskite Solar Cells. *Adv. Mater. Interfaces* **2016**, *3*, 1600327. [[CrossRef](#)]
11. Zhao, P.; Lin, Z.; Wang, J.; Yue, M.; Su, J.; Zhang, J.; Chang, J.; Hao, Y. Numerical Simulation of Planar Heterojunction Perovskite Solar Cells Based on SnO₂ Electron Transport Layer. *ACS Appl. Energy Mater.* **2019**, *2*, 4504–4512. [[CrossRef](#)]
12. Sharma, R.; Sharma, A.; Agarwal, S.; Dhaka, M.S. Stability and Efficiency Issues, Solutions and Advancements in Perovskite Solar Cells: A Review. *Sol. Energy* **2022**, *244*, 516–535. [[CrossRef](#)]
13. Jung, H.S.; Han, G.S.; Park, N.-G.; Ko, M.J. Flexible Perovskite Solar Cells. *Joule* **2019**, *3*, 1850–1880. [[CrossRef](#)]

14. Feng, J.; Zhu, X.; Yang, Z.; Zhang, X.; Niu, J.; Wang, Z.; Zuo, S.; Priya, S.; Liu, S.; Yang, D. Record Efficiency Stable Flexible Perovskite Solar Cell Using Effective Additive Assistant Strategy. *Adv. Mater.* **2018**, *30*, 1801418. [[CrossRef](#)]
15. Kiani, M.S.; Sadirkhanov, Z.T.; Kakimov, A.G.; Parkhomenko, H.P.; Ng, A.; Jumabekov, A.N. Solution-Processed SnO₂ Quantum Dots for the Electron Transport Layer of Flexible and Printed Perovskite Solar Cells. *Nanomaterials* **2022**, *12*, 2615. [[CrossRef](#)]
16. Giacomo, F.D.; Fakharuddin, A.; Jose, R.; Brown, T.M. Progress, Challenges and Perspectives in Flexible Perovskite Solar Cells. *Energy Environ. Sci.* **2016**, *9*, 3007–3035. [[CrossRef](#)]
17. Gao, Y.; Huang, K.; Long, C.; Ding, Y.; Chang, J.; Zhang, D.; Etgar, L.; Liu, M.; Zhang, J.; Yang, J. Flexible Perovskite Solar Cells: From Materials and Device Architectures to Applications. *ACS Energy Lett.* **2022**, *7*, 1412–1445. [[CrossRef](#)]
18. Samantaray, N.; Parida, B.; Soga, T.; Sharma, A.; Kapoor, A.; Najjar, A.; Singh, A. Recent Development and Directions in Printed Perovskite Solar Cells. *Phys. Status Solidi A* **2022**, *219*, 2100629. [[CrossRef](#)]
19. Sutherland, L.J.; Vak, D.; Gao, M.; Peiris, T.A.N.; Jasieniak, J.; Simon, G.P.; Weerasinghe, H. Vacuum-Free and Solvent-Free Deposition of Electrodes for Roll-to-Roll Fabricated Perovskite Solar Cells. *Adv. Energy Mater.* **2022**, *12*, 2202142. [[CrossRef](#)]
20. Othman, M.; Zheng, F.; Seeber, A.; Chesman, A.S.R.; Scully, A.D.; Ghiggino, K.P.; Gao, M.; Etheridge, J.; Angmo, D. Millimeter-Sized Clusters of Triple Cation Perovskite Enables Highly Efficient and Reproducible Roll-to-Roll Fabricated Inverted Perovskite Solar Cells. *Adv. Funct. Mater.* **2022**, *32*, 2110700. [[CrossRef](#)]
21. Liu, Q.; Cai, W.; Wang, W.; Wang, H.; Zhong, Y.; Zhao, K. Controlling Phase Transition toward Future Low-Cost and Eco-Friendly Printing of Perovskite Solar Cells. *J. Phys. Chem. Lett.* **2022**, *13*, 6503–6513. [[CrossRef](#)] [[PubMed](#)]
22. Parida, B.; Singh, A.; Kalathil Soopy, A.K.; Sangaraju, S.; Sundaray, M.; Mishra, S.; Liu, S.; Najjar, A. Recent Developments in Upscalable Printing Techniques for Perovskite Solar Cells. *Adv. Sci.* **2022**, *9*, 2200308. [[CrossRef](#)] [[PubMed](#)]
23. Gong, C.; Fan, B.; Li, F.; Xing, Z.; Meng, X.; Hu, T.; Hu, X.; Chen, Y. An Enhanced Couette Flow Printing Strategy to Recover Efficiency Losses by Area and Substrate Differences in Perovskite Solar Cells. *Energy Environ. Sci.* **2022**, *15*, 4313–4322. [[CrossRef](#)]
24. Meng, F.; Gao, L.; Yan, Y.; Cao, J.; Wang, N.; Wang, T.; Ma, T. Ultra-Low-Cost Coal-Based Carbon Electrodes with Seamless Interfacial Contact for Effective Sandwich-Structured Perovskite Solar Cells. *Carbon* **2019**, *145*, 290–296. [[CrossRef](#)]
25. Shalenov, E.O.; Dzhumagulova, K.N.; Seitkozhanov, Y.S.; Ng, A.; Valagiannopoulos, C.; Jumabekov, A.N. Insights on Desired Fabrication Factors from Modeling Sandwich and Quasi-Interdigitated Back-Contact Perovskite Solar Cells. *ACS Appl. Energy Mater.* **2021**, *4*, 1093–1107. [[CrossRef](#)]
26. Jumabekov, A.N.; Gaspera, E.D.; Xu, Z.-Q.; Chesman, A.S.R.; van Embden, J.; Bonke, S.A.; Bao, Q.; Vak, D.; Bach, U. Back-Contacted Hybrid Organic–Inorganic Perovskite Solar Cells. *J. Mater. Chem. C* **2016**, *4*, 3125–3130. [[CrossRef](#)]
27. Shalenov, E.O.; Seitkozhanov, Y.S.; Valagiannopoulos, C.; Ng, A.; Dzhumagulova, K.N.; Jumabekov, A.N. Performance Evaluation of Different Designs of Back-Contact Perovskite Solar Cells. *Sol. Energy Mater. Sol. Cells* **2022**, *234*, 111426. [[CrossRef](#)]
28. Parkhomenko, H.P.; Shalenov, E.O.; Umatova, Z.; Dzhumagulova, K.N.; Jumabekov, A.N. Fabrication of Flexible Quasi-Interdigitated Back-Contact Perovskite Solar Cells. *Energies* **2022**, *15*, 3056. [[CrossRef](#)]
29. Prince, K.J.; Nardone, M.; Dunfield, S.P.; Teeter, G.; Mirzokarimov, M.; Warren, E.L.; Moore, D.T.; Berry, J.J.; Wolden, C.A.; Wheeler, L.M. Complementary Interface Formation toward High-Efficiency All-Back-Contact Perovskite Solar Cells. *Cell Rep. Phys. Sci.* **2021**, *2*, 100363. [[CrossRef](#)]
30. Wong-Stringer, M.; Routledge, T.J.; McArdle, T.; Wood, C.J.; Game, O.S.; Smith, J.A.; Bishop, J.E.; Vaenas, N.; Coles, D.M.; Buckley, A.R.; et al. A Flexible Back-Contact Perovskite Solar Micro-Module. *Energy Environ. Sci.* **2019**, *12*, 1928–1937. [[CrossRef](#)]
31. Liu, J.; Wang, D.; Zhang, Y.; Chen, K.; She, B.; Liu, B.; Zhang, Z.; Huang, Y.; Xiong, J.; Zhang, H.; et al. Room-Temperature-Processed, Carbon-Based Fully Printed Mesoscopic Perovskite Solar Cells with 15% Efficiency. *Sol. RRL* **2021**, *5*, 2100274. [[CrossRef](#)]
32. Maity, K.; Pal, U.; Mishra, H.K.; Maji, P.; Sadhukhan, P.; Mallick, Z.; Das, S.; Mondal, B.; Mandal, D. Piezo-Phototronic Effect in Highly Stable CsPbI₃-PVDF Composite for Self-Powered Nanogenerator and Photodetector. *Nano Energy* **2022**, *92*, 106743. [[CrossRef](#)]
33. Zhou, Y.; Zhao, Y. Chemical Stability and Instability of Inorganic Halide Perovskites. *Energy Environ. Sci.* **2019**, *12*, 1495–1511. [[CrossRef](#)]
34. Lin, X.; Chesman, A.S.R.; Raga, S.R.; Scully, A.D.; Jiang, L.; Tan, B.; Lu, J.; Cheng, Y.-B.; Bach, U. Effect of Grain Cluster Size on Back-Contact Perovskite Solar Cells. *Adv. Funct. Mater.* **2018**, *28*, 1805098. [[CrossRef](#)]
35. Fahrenbruch, A.; Bube, R. *Fundamentals of Solar Cells: Photovoltaic Solar Energy Conversion*; Elsevier: Amsterdam, The Netherlands, 2012; ISBN 978-0-323-14538-1.
36. Pockett, A.; Eperon, G.E.; Peltola, T.; Snaith, H.J.; Walker, A.; Peter, L.M.; Cameron, P.J. Characterization of Planar Lead Halide Perovskite Solar Cells by Impedance Spectroscopy, Open-Circuit Photovoltage Decay, and Intensity-Modulated Photovoltage/Photocurrent Spectroscopy. *J. Phys. Chem. C* **2015**, *119*, 3456–3465. [[CrossRef](#)]
37. Brus, V.V.; Lang, F.; Bundesmann, J.; Seidel, S.; Denker, A.; Rech, B.; Landi, G.; Neitzert, H.C.; Rappich, J.; Nickel, N.H. Defect Dynamics in Proton Irradiated CH₃NH₃PbI₃ Perovskite Solar Cells. *Adv. Electron. Mater.* **2017**, *3*, 1600438. [[CrossRef](#)]
38. Zaban, A.; Greenshtein, M.; Bisquert, J. Determination of the Electron Lifetime in Nanocrystalline Dye Solar Cells by Open-Circuit Voltage Decay Measurements. *ChemPhysChem* **2003**, *4*, 859–864. [[CrossRef](#)]
39. Lei, Y.; Xu, Y.; Wang, M.; Zhu, G.; Jin, Z. Origin, Influence, and Countermeasures of Defects in Perovskite Solar Cells. *Small* **2021**, *17*, 2005495. [[CrossRef](#)]
40. Sze, S.M.; Li, Y.; Ng, K.K. *Physics of Semiconductor Devices*; John Wiley & Sons: Hoboken, NJ, USA, 2021; ISBN 978-1-119-61800-3.

41. Ball, J.M.; Petrozza, A. Defects in Perovskite-Halides and Their Effects in Solar Cells. *Nat. Energy* **2016**, *1*, 16149. [[CrossRef](#)]
42. Wang, F.; Bai, S.; Tress, W.; Hagfeldt, A.; Gao, F. Defects Engineering for High-Performance Perovskite Solar Cells. *NPJ Flex. Electron.* **2018**, *2*, 22. [[CrossRef](#)]
43. Aharon, S.; Gamliel, S.; El Cohen, B.; Etgar, L. Depletion Region Effect of Highly Efficient Hole Conductor Free $\text{CH}_3\text{NH}_3\text{PbI}_3$ Perovskite Solar Cells. *Phys. Chem. Chem. Phys.* **2014**, *16*, 10512–10518. [[CrossRef](#)] [[PubMed](#)]
44. Ishikawa, R.; Watanabe, S.; Yamazaki, S.; Oya, T.; Tsuboi, N. Perovskite/Graphene Solar Cells without a Hole-Transport Layer. *ACS Appl. Energy Mater.* **2019**, *2*, 171–175. [[CrossRef](#)]
45. Huang, Y.; Liu, T.; Liang, C.; Xia, J.; Li, D.; Zhang, H.; Amini, A.; Xing, G.; Cheng, C. Towards Simplifying the Device Structure of High-Performance Perovskite Solar Cells. *Adv. Funct. Mater.* **2020**, *30*, 2000863. [[CrossRef](#)]
46. Lin, X.; Jumabekov, A.N.; Lal, N.N.; Pascoe, A.R.; Gómez, D.E.; Duffy, N.W.; Chesman, A.S.R.; Sears, K.; Fournier, M.; Zhang, Y.; et al. Dipole-Field-Assisted Charge Extraction in Metal-Perovskite-Metal Back-Contact Solar Cells. *Nat. Commun.* **2017**, *8*, 613. [[CrossRef](#)]
47. Sadollahkhani, A.; Liu, P.; Leandri, V.; Safdari, M.; Zhang, W.; Gardner, J.M. Energetic Barriers to Interfacial Charge Transfer and Ion Movement in Perovskite Solar Cells. *ChemPhysChem* **2017**, *18*, 3047–3055. [[CrossRef](#)]
48. Duan, L.; Uddin, A. Defects and Stability of Perovskite Solar Cells: A Critical Analysis. *Mater. Chem. Front.* **2022**, *6*, 400–417. [[CrossRef](#)]
49. Wang, Z.; Zeng, L.; Zhang, C.; Lu, Y.; Qiu, S.; Wang, C.; Liu, C.; Pan, L.; Wu, S.; Hu, J.; et al. Rational Interface Design and Morphology Control for Blade-Coating Efficient Flexible Perovskite Solar Cells with a Record Fill Factor of 81%. *Adv. Funct. Mater.* **2020**, *30*, 2001240. [[CrossRef](#)]
50. Kim, Y.Y.; Yang, T.-Y.; Suhonen, R.; Välimäki, M.; Maaninen, T.; Kemppainen, A.; Jeon, N.J.; Seo, J. Gravure-Printed Flexible Perovskite Solar Cells: Toward Roll-to-Roll Manufacturing. *Adv. Sci.* **2019**, *6*, 1802094. [[CrossRef](#)]
51. Gao, L.-L.; Li, C.-X.; Li, C.-J.; Yang, G.-J. Large-Area High-Efficiency Perovskite Solar Cells Based on Perovskite Films Dried by the Multi-Flow Air Knife Method in Air. *J. Mater. Chem. A* **2017**, *5*, 1548–1557. [[CrossRef](#)]
52. Azam, M.; Khan, A.A.; Liang, G.-X.; Li, G.-J.; Chen, S.; Zheng, Z.-H.; Farooq, U.; Ishaq, M.; Fan, P.; Wang, Z.; et al. Examining the Interfacial Defect Passivation with Chlorinated Organic Salt for Highly Efficient and Stable Perovskite Solar Cells. *Sol. RRL* **2020**, *4*, 2000358. [[CrossRef](#)]
53. Bacal, D.M.; Lal, N.N.; Jumabekov, A.N.; Hou, Q.; Hu, Y.; Lu, J.; Chesman, A.S.R.; Bach, U. Solution-Processed Antireflective Coating for Back-Contact Perovskite Solar Cells. *Opt. Express* **2020**, *28*, 12650–12660. [[CrossRef](#)]
54. Yang, Z.; Yang, W.; Yang, X.; Greer, J.C.; Sheng, J.; Yan, B.; Ye, J. Device Physics of Back-Contact Perovskite Solar Cells. *Energy Environ. Sci.* **2020**, *13*, 1753–1765. [[CrossRef](#)]

Disclaimer/Publisher's Note: The statements, opinions and data contained in all publications are solely those of the individual author(s) and contributor(s) and not of MDPI and/or the editor(s). MDPI and/or the editor(s) disclaim responsibility for any injury to people or property resulting from any ideas, methods, instructions or products referred to in the content.